

# PROCEEDINGS OF SPIE

[SPIDigitalLibrary.org/conference-proceedings-of-spie](https://SPIDigitalLibrary.org/conference-proceedings-of-spie)

## Fast quasi-static beam steering via conformally-mapped gratings

Liang Wu, William Maxwell Mellette, Glenn M. Schuster, Joseph E. Ford

Liang Wu, William Maxwell Mellette, Glenn M. Schuster, Joseph E. Ford, "Fast quasi-static beam steering via conformally-mapped gratings," Proc. SPIE 11136, Optics and Photonics for Information Processing XIII, 111360W (6 September 2019); doi: 10.1117/12.2529460

**SPIE.**

Event: SPIE Optical Engineering + Applications, 2019, San Diego, California, United States

# Fast Quasi-static Beam Steering via Conformally-Mapped Gratings

Liang Wu<sup>a,b</sup>, William Maxwell Mellette<sup>b</sup>, Glenn M. Schuster<sup>b</sup>, and Joseph E. Ford<sup>\*b</sup>

<sup>a</sup>School of Physics, University of Electronic Science and Technology of China, Chengdu 610054, China

<sup>b</sup>Department of Electrical and Computer Engineering, University of California San Diego, La Jolla, CA 92093, USA

## ABSTRACT

Fast beam steering is useful in applications including free space optical switching and communications. Quasi-static beam steering, where the beam rapidly switches between discrete fixed directions, presents special challenges. Here we demonstrate a fast quasi-static ‘pinwheel’ scanner by conformally mapping linear blazed gratings into curved structures fabricated onto annular sections of a rotary disk. We use Matlab and Zemax to model the effects of the conformally-mapped grating on the emitted optical beam. We show a specific two-dimensional (2D) ‘pinwheel’ scanner design with 56 gratings, each deflecting 1.31  $\mu\text{m}$  incident light by 11.3° in one of four directions with 75% optical efficiency. The element was fabricated by optical grey-scale lithography on a 95 mm diameter substrate, coated with gold, and mounted onto the spindle of a 3.5” format 7200 rpm magnetic disk drive. We characterize the optical beam steering efficiency, pointing, and stability, and demonstrate microsecond switching speed of a single mode fiber signal.

**Keywords:** Quasi-static beam steering; Conformal mapping; Diffraction grating; Pinwheel scanner.

## 1. INTRODUCTION

In recent years, optical beam steering technology has been developed for a broad range of applications including projection displays, optical switching, Lidar, and laser communications<sup>1–5</sup> using technologies such as micro-electromechanical systems (MEMS),<sup>6</sup> liquid crystal on silicon (LCoS),<sup>7</sup> and silicon photonic optical phased arrays.<sup>8</sup> The working mode of beam steering systems can be divided into point-to-point scanning, line-to-line continuous scanning, and arbitrary scanning. The extreme of point-to-point scanning can be called quasi-static beam steering, where the scanner has to reach and stay at a desired angle, then discontinuously switch to each new angle. Ideally the beam switching is very rapid, and the intermediate beam dwelling can be regarded as a relative equilibrium state.<sup>9</sup>

Currently popular beam steerers such as MEMS tilt mirrors and LCoS can provide programmable continuous beam control, but have difficulty in realizing fast quasi-static beam steering due to the fundamental tradeoff between speed, resolution, and optical aperture. For MEMS tilt mirrors operating at quasi-static mode under a non-resonant state, relatively low mechanical robustness will limit the scanning range and dynamic trajectory scanning.<sup>10,11</sup> For LCoS devices, their switching speed is only on the order of sub-milliseconds, and apertures are smaller than several centimeters.<sup>12,13</sup> This challenge can be mitigated when, as in many beam steering applications, the scanning trajectory is repetitive and requires only a sequence of beam deflection states. In this case we can revisit some historic beam scanning systems, rotating diffraction gratings or polygons, which have been used to provide nearly linear scanning using a rotational faceted beam scanner. However, flat mirror facets or straight diffraction gratings do not provide perfect quasi-static pointing, as the beam wanders under rotation of each facet.<sup>14–16</sup> Here, we propose a novel quasi-static ‘pinwheel’ scanner by *conformally mapping* linear blazed gratings into curved surface relief structures fabricated onto regions of a rotary disk. We show experimental results for a 1.3 $\mu\text{m}$  beam deflector using a 95 mm disk rotating at 7200 rpm, and demonstrate this method enables accurate and fast quasi-static beam steering.

## 2. THEORY

Figure 1 shows the conceptual design of our quasi-static beam scanner. It consists of a rotating disk substrate with a sequence of grating sectors which is mounted onto a spindle. The entire surface of the disk can be divided into a number of annular tracks (one track shown in Fig. 1), with many grating sectors defined in each track. A blazed grating with

specific grating period is fabricated in each grating sector to realize beam diffraction in different angles. The laser delivered onto the grating sector will be deflected, then switched between the pre-programmed directions as the disk is rotated to illuminate subsequent grating sectors. The arc length of the grating sectors (and the rotation speed) determines the duration the beam illuminates each sector, setting how long the beam dwells in each direction. If the center of the annular track is at the radius of  $R_0$ , and the annular track is evenly divided into  $N$  grating sectors, then the arc length of a grating sector at  $R_0$  will be  $L_{arc} = 2\pi R_0 / N$ . For the disk with rotating speed of  $n$  rpm (revolutions per minute), the beam dwelling time must be  $t_{dwell} = L_{arc} / (2\pi R_0 \cdot n) = 1 / Nn$ . The transition time depends on the area illuminated. For an incident Gaussian beam with waist  $w_0$ , the beam switching time can be approximated as  $t \approx 2w_0 / (2\pi R_0 \cdot n)$ .

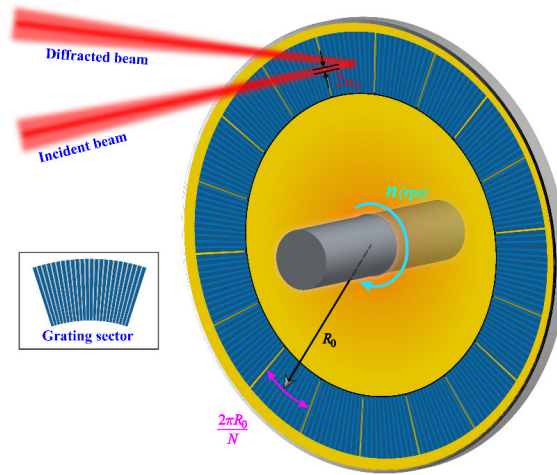


Figure 1. Conceptual diagram of quasi-static beam scanner ‘pinwheel’.

A beam scanner using regions of straight (ruled) blazed gratings is superior to flat angled facets in that the beam deflection occurs at a fixed depth, independent of rotation angle. However, regions of straight gratings do not provide true quasi-static steering. Grating rotation within each sub-sector causes the beam to follow a shallow arc, resulting in an error with beam deflection. Consider a one-dimensional linear grating with grating period of  $T_0$  (or frequency  $f_0$ ). When the scanner is rotated, the direction of grating line will also be changed relative to the original coordinate system. The varied grating period after rotation is determined by the projection of  $T_0$ , which means the deflection angle will vary with the rotation angle of the disk. The method we use to overcome this problem is conformal mapping,<sup>17</sup> which is a mathematical process to transform a straight grating into a curved grating so that the orientation of the curved grating lines will match the annular region of the disk. A schematic diagram of the conformal mapping method is shown in Fig.2. Here, a rectangle with sides  $W_0$  and  $L_0$  is transformed into a sector, and the sector is mapped onto a disk with diameter of  $D_0$  and at the radial position of  $R_0$ . The rectangular domain is defined as  $\mathbf{R}$ , with coordinates  $(w, l) \in \mathbf{R}$ . The target circular disk domain is defined as  $\mathbf{D}$ , with coordinates  $(u, v) \in \mathbf{D}$ . An intermediate domain  $\mathbf{\Omega}$  is used for calculation which is converted by normalizing the rectangular domain to  $R_0$ , and the coordinates are expressed as

$$\begin{cases} x = \frac{w}{R_0} \\ y = \frac{l}{R_0} - \frac{L_0}{2R_0} \end{cases} \quad (1)$$

Eq. (1) represents a transformation relationship between the rectangular domain  $\mathbf{R}$  and intermediate domain  $\mathbf{\Omega}$  under different values of  $R_0$ , and note that  $R_0$  is the radial position where the center of the sector will be located. The intermediate domain is still on the positive side of the y axis, but it is symmetric with respect to the x axis.

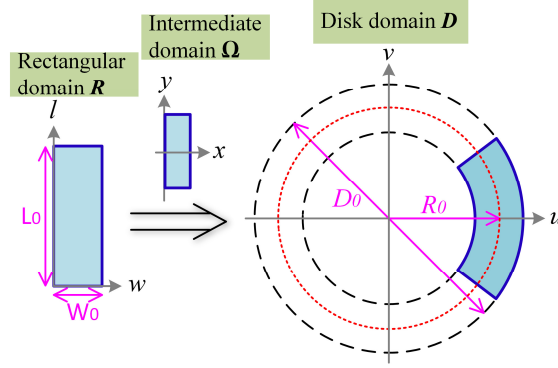


Figure 2. Schematic diagram of conformal mapping method.

Then we set up two complex variables to represent the coordinates of intermediate domain  $\Omega$  and disk domain  $D$ :  $z = x + iy$  and  $m = u + iv$ . From an analytic point of view, a complex function relationship  $f$  should be taken to conformally map the point  $z = x + iy$  belonging to the intermediate domain  $\Omega$  to the point  $m = u + iv$  belonging to the disk domain  $D$ , namely  $m = f(z)$ . According to the theory of conformal mapping, an explicit function of conformal map with the desired properties is the exponential map:<sup>18</sup>

$$f(z) = R_0 e^{z - L_x}, \quad (2)$$

where  $L_x = \frac{W_0}{2R_0}$ . Substituting  $m$  and  $z$  into Eq. (2), we can derive that

$$\begin{cases} u = R_0 e^{x - L_x} \cdot \cos y \\ v = R_0 e^{x - L_x} \cdot \sin y \end{cases} \quad (3)$$

Combining Eq. (3) with Eq. (1), we can get a one-to-one map between the rectangular domain  $R$  and disk domain  $D$ . We can now transform a rectangular domain of any size into an annular sector on a disk with any diameter. In this paper, the purpose of the conformal mapping method is to achieve a constant local grating period with respect to the disk rotation. This requires the orientation of the grating grooves and the angle to be preserved locally. In fact, this is the key feature of angle-preserving transformation of the conformal mapping method.

### 3. SIMULATION

Based on the conformal mapping method, we use the numerical software Matlab to calculate the desired conformal grating patterns, and use the optical design software Zemax to model the conformal grating based ‘pinwheel’ scanner and verify the deflection angle under disk rotation with different beam properties.

#### 3.1 Matlab numerical calculations

As an example, assume that a rectangular grating section of width  $W_0 = 0.1$  mm and length  $L_0 = 0.2$  mm needs to be mapped. Fig. 3(a) shows the rectangle and its grid distribution, the small circles represent the points of the grid. Letting the diameter of a target disk be  $D_0 = 1.0$  mm and the center of grating sector be  $R_0 = (D_0 - W_0)/2 = 0.45$  mm, the sector will be close to the perimeter of the disk. The transformed sector calculated by the conformal mapping method is shown in Fig. 3(b). As we can see, the center of the sector is at the radial position of 0.45 mm of the disk, the radius of the inner circle is  $R_0 e^{-\frac{W_0}{2R_0}}$ , and the radius of the outer circle is  $R_0 e^{\frac{W_0}{2R_0}}$ . All the grid points in the rectangular domain are one-to-one mapped to the corresponding position in the disk domain. Importantly, the points are no longer distributed along the

horizontal or vertical direction, but along the radial direction. Each point is at the intersection of the radial and tangential directions, which ensures the angle between the points to be  $90^\circ$  in the disk domain.

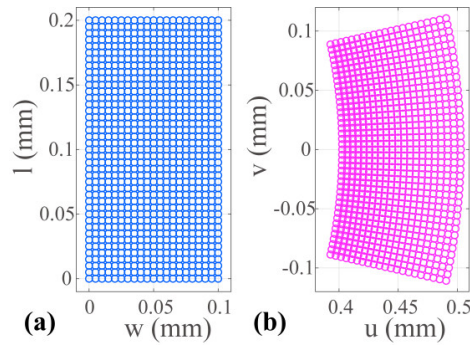


Figure 3 Grid distribution in (a) Rectangular domain and (b) Disk domain.

The grating is conformally mapped from the rectangular domain to the target disk domain as we obtain the mapping relationship of the grids. In Fig. 4, the upper row shows the phase patterns of linear gratings with different orientations, and the lower row shows the corresponding conformal gratings generated by the conformal mapping method. Herein, the grating period is  $6.7 \mu\text{m}$ , the red arrows indicate the local grating orientation (grating-vector direction), and the orientations are  $0^\circ$ ,  $45^\circ$ ,  $90^\circ$  and  $135^\circ$  respectively. Comparing two rows of phase patterns, we can clearly see that the orientation will change as the linear grating is rotated. However, for the conformal grating, the grating curves are not parallel to the y-axis any more. They are stretched to fit the radial position, resulting in the same orientation when the grating is rotated about the center of the disk. If a large fraction of one of these conformally mapped gratings were illuminated, the diffracted wavefront would be significantly distorted. But by assumption in the quasi-static beam steering system, only a small region is illuminated. In that small area the grating facets are approximately linear, and the diffracted wavefront is similar to that which would be generated by a straight grating.

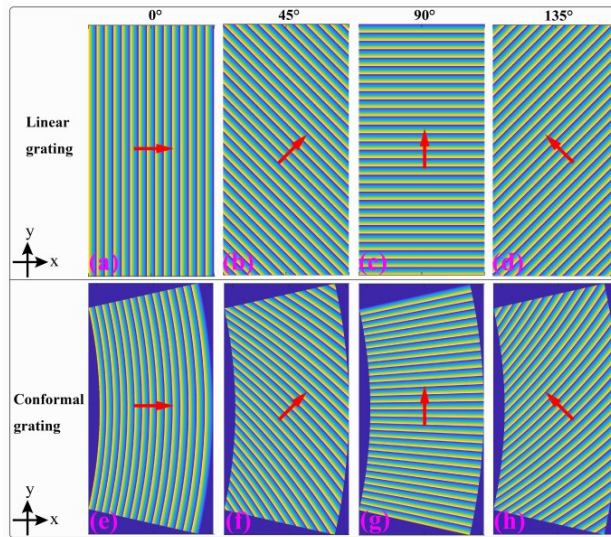


Figure 4. Phase patterns of linear grating and conformal grating. (a)-(d) Linear gratings with grating orientation of  $0^\circ$ ,  $45^\circ$ ,  $90^\circ$ , and  $135^\circ$ . (e)-(h) Corresponding conformal gratings mapped from the linear gratings in (a)-(d).

### 3.2 Zemax optical modeling

The conformal grating performance can be simulated by the popular commercial program Zemax OpticStudio. OpticStudio allows users to customize new types of surfaces not covered by the Zemax built-in surface library using a flexible function:

the User-Defined Surface (UDS). The properties of the surface are defined in a separate C++ program, compiled into a code file, and linked into Zemax dynamically via the Windows Dynamic Link Library (DLL).<sup>19</sup> Here we describe the UDS implementation of our particular conformal grating surface based on the theoretical model described above and in combination with the Zemax design methodology. Once the conformal grating surface is modeled in Zemax, it can be integrated into the subsequent design of the overall optical system.

A diffractive surface (i.e. diffraction grating) in Zemax bends rays according to the grating equation:<sup>20</sup>

$$n_2 \sin \theta_2 - n_1 \sin \theta_1 = m\lambda / T_0 \quad (4)$$

where  $m$  is the diffraction order,  $\theta_2$  is the diffracted angle,  $\theta_1$  is the incident angle,  $n_1$  and  $n_2$  are the refraction indices before and after the grating, respectively.  $\lambda$  is the wavelength and  $T_0$  is the grating period. When rays pass through the grating surface, Zemax will deviate the rays by the derivatives of the phase as a function of  $x$  and  $y$ , and the optical path length is modified to include the phase change, which are realized by

$$\begin{aligned} l' &= l + \frac{\lambda}{2\pi} \frac{\partial \phi}{\partial x} \\ m' &= m + \frac{\lambda}{2\pi} \frac{\partial \phi}{\partial y} \end{aligned} \quad (5)$$

where  $l$  and  $m$  are the direction cosines,  $\phi$  is the phase,  $x$  and  $y$  are the coordinates in Zemax. Thus, the key to model the conformal grating is defining the phase and phase derivatives. For a one-dimensional linear diffraction grating, i.e. with grating lines parallel to the  $x$ -axis, the grating period is constant and the phase will be  $\phi = k_0 \frac{m\lambda}{T_0} \cdot y$ , where  $k_0 = 2\pi/\lambda$  is

the wave number. Then the derivatives of the phase of  $x$  and  $y$  directions are:  $\frac{\partial \phi}{\partial x} = 0$ ,  $\frac{\partial \phi}{\partial y} = k_0 m\lambda / T_0$ . For the conformal grating, the grating period is no longer constant but a function of both  $x$  and  $y$  directions. However, the grating period of conformal grating is radially symmetric: it is equal at same radius and varies only with the radial position. This change could be derived from the conformal mapping equations of Eq. (3), when we let  $y$  equals to 0,  $u$  to be equal to  $r$ , then we can obtain the differentiate of  $r$  with respect to  $w$ :

$$\frac{dr}{dw} = \exp(w / R_0 - W_0 / 2R_0). \quad (6)$$

where  $r$  is the radial coordinate on the disk, and  $r = \sqrt{x^2 + y^2}$ . Substituting  $w = R_0 \cdot [\ln(r / R_0) + W_0 / 2R_0]$  into the above equation simplifies it as

$$\frac{dr}{dw} = r / R_0 \quad (7)$$

If we note that the change of grating period is caused by the change of position, then the stretched grating period of conformal grating can be defined as

$$T_s = T_0 \cdot \frac{dr}{dw} = T_0 \cdot \frac{r}{R_0} \quad (8)$$

where  $T_0$  is the original grating period before conformal mapping. According to the grating equation, we have

$$\frac{\Delta \phi_s}{\Delta r} = \frac{2\pi}{\lambda} \cdot \frac{m\lambda}{T_s} = 2\pi \frac{R_0}{T_0} \frac{1}{r} \quad (9)$$

Finally, we integrate Eq. (9) along  $r$ , the phase of the conformal grating becomes

$$\phi_s = 2\pi \cdot \frac{R_0}{T_0} \ln\left(\frac{r}{r_{in}}\right) \quad (10)$$

Here,  $r_{in}$  is the inner radius, namely  $R_0 e^{-\frac{W_0}{2R_0}}$ . For any disk diameter and original grating period, Eqs. (8) and (10) will be applied to create the UDS of conformal grating, the stretched grating period and phase are calculated automatically in Zemax when the UDS is called.

In Zemax, we generated an example conformal grating disk with diameter of 0.4 mm, where the original grating period is 6.7  $\mu\text{m}$ . Figure 5(a) shows the phase profile of the defined conformal grating disk which is computed by Zemax Analysis capability of surface phase. The red arrows indicate the grating orientations of corresponding sectors. The phases are displayed modulo- $2\pi$ . We also made a comparison between the calculation of phase in the Matlab simulation and by the Zemax modeling. Fig. 5(b) shows the cross section of phase along the positive x-axis (marked by black bar in Fig. 5(a)). The phase profiles are almost similar, verifying that the Zemax modeling yields the same result as the Matlab calculation. In fact, the direct calculation of phase in Zemax is also based on the conformal mapping formula discussed in Section 2.

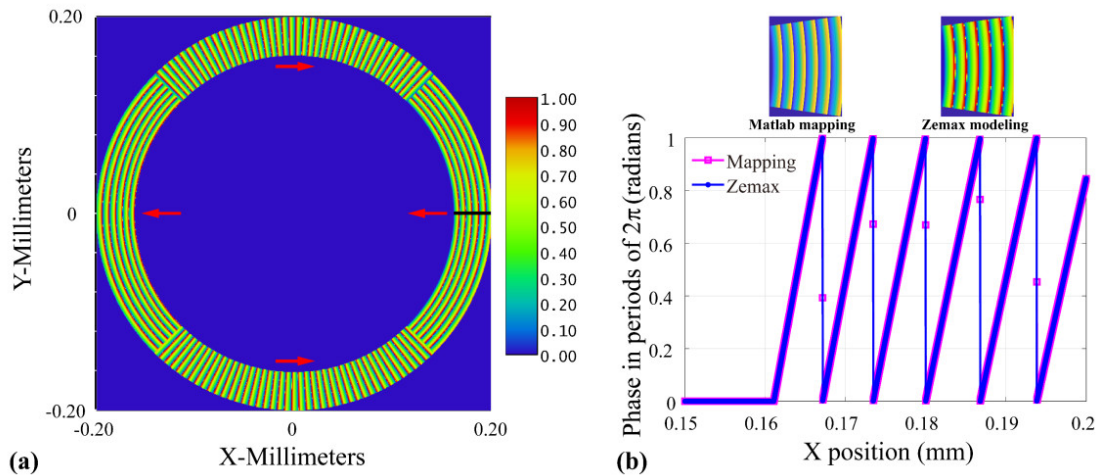


Figure 5. (a) Surface phase map of conformal grating disk in Zemax. (b) Comparison between the calculation of phase in the Matlab simulation and by the Zemax modeling.

Due to the resolution limitation of the display methods available in Zemax, the phase map above exhibits only a very small disk diameter of 0.4 mm. The 3D optical layout of the linear grating disk and the conformal grating disk are shown in Fig. 6 (a) and (b), where a 20 mm disk diameter is used. The light source is collimated onto the gratings by Lens 1, deflected by the gratings then focused on the image plane by Lens 2. Here, the input beam size is 1.0 mm, the radial width of annular grating regions is 1.0 mm, and the central position of both annular grating regions is  $R_0 = 9.5$  mm (close to the edge of the disk). The inserted spot diagrams illustrate the corresponding illuminated beam spots at two positions. The upper one is the collimated beam in front of Lens 2, and the lower one is the focused beam on the image plane. Blue, green, and red colors indicate the beam spots when the gratings are centered, rotated by  $10^\circ$ , and rotated by  $-10^\circ$  respectively. It is apparent that when the linear grating is rotated, the beam is shifted and is not focused at the same direction after passing through the Lens 2. However, in Fig. 6(b), we can see the collimated and focused beams are kept at the same direction no matter how the conformal grating is rotated. The deflection angle of the rays in the X and Y directions after diffraction from the gratings were also captured using the Zemax built-in operands REAA and REAB. Figure 6(c) shows the relationship between the deflection angle and the disk rotation, where the desired steering angle is  $11.33^\circ$  in the Y direction. These results also expose the problem of ray deviation of the rotational linear grating, while the ray does not wander for the conformal grating. In Fig. 6(b), it can be seen that the beam spot from the conformal grating becomes a little larger and the shape is not totally round, so the beam is stretched by the curved grating lines of the conformal grating. When the

radius of the disk is smaller, the beam distortion will be more pronounced. Figure 6(d) shows the variation of the RMS (root-mean-square) wavefront error with disk radius under different incident beam sizes. The inserted spot diagrams are the focused beam spots of three beam sizes when the disk diameter is 80 mm, as marked in the dashed ellipse. As we can see, the RMS wavefront error decreases with the increase of the disk size. When the diameter of the disk arrives a certain value, the RMS wavefront error will not change significantly. And the smaller the beam size, the smaller the RMS wavefront error, i.e., when the beam size is 0.5 mm and the disk radius is larger than 40 mm, the RMS wavefront error will approach zero.

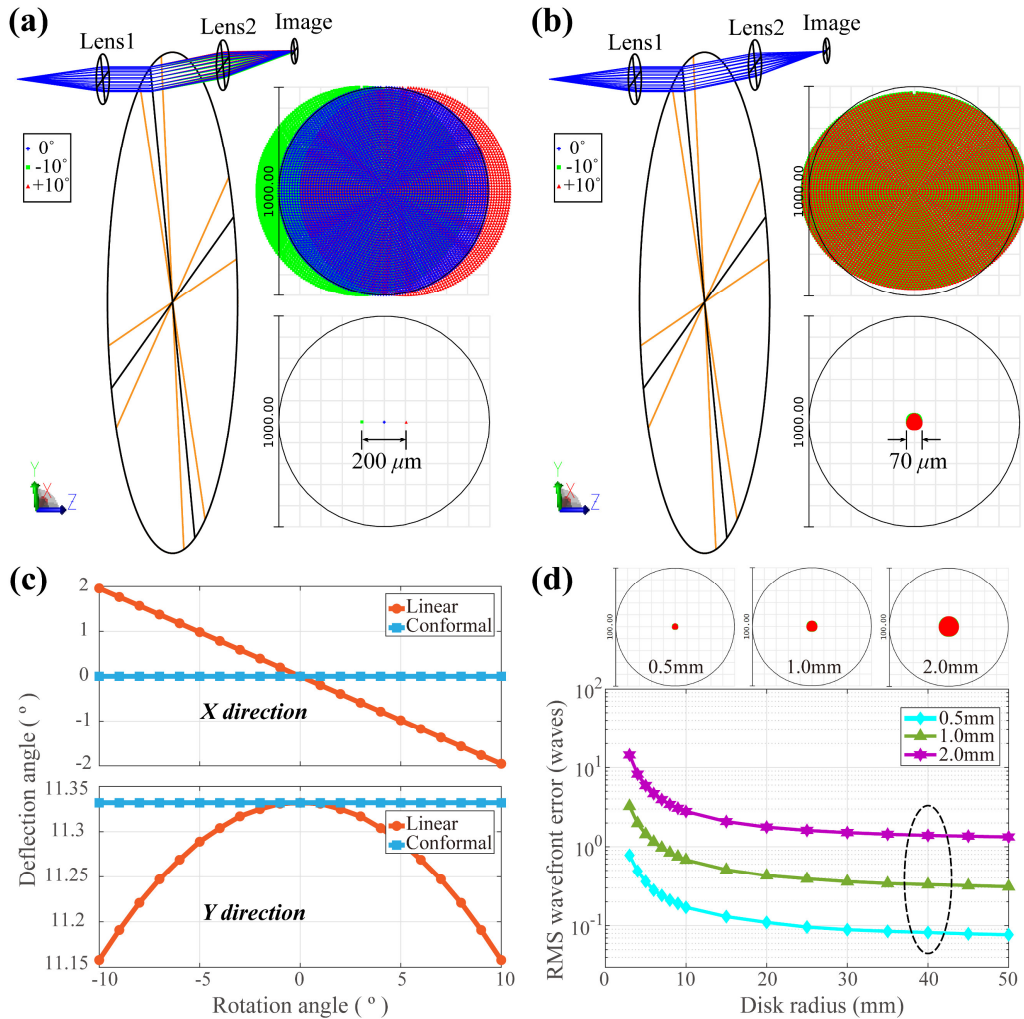


Figure 6. 3D layout and spot diagram of (a) Linear grating disk; (b) Conformal grating disk; (c) The relationship between the deflection angle and the disk rotation; (d) The relationship between the RMS wavefront error and the disk radius (logarithmic plot for the vertical axis).

#### 4. DESIGN AND EXPERIMENTAL RESULTS

Figure 7(a) shows the conformal grating element ‘pinwheel’, which is fabricated by grayscale laser writing (HEIDELBERG DWL 66+, resolution: 200nm) on a substrate of a hard-drive disk with 95 mm diameter. We defined 10 annular grating regions on the disk, including 4 wide tracks and two groups of narrow tracks (each group has 3 tracks). Each track consists of 56 grating sectors and patterned with 4 kinds of orientations (each orientation occupies 14 grating sectors), realizing beam steering in four directions (up, right, down, and left) periodically when the incident beam hits a fixed position on the disk. The grating frequency is 150 lines/mm, so the grating period is 6.67 μm, and the blaze angle is

5.67°, so that the steering angle is 11.33°. A gold layer is sputtered on the surface of the grating to provide high reflectivity at the design wavelength of 1310 nm. Before laser writing the grating features, the position of the disk was precisely aligned to center the annular grating area on the disk. The fabricated disk is mounted on a spindle and driven by the hard-drive motor, which can spin up to 7200 rpm.

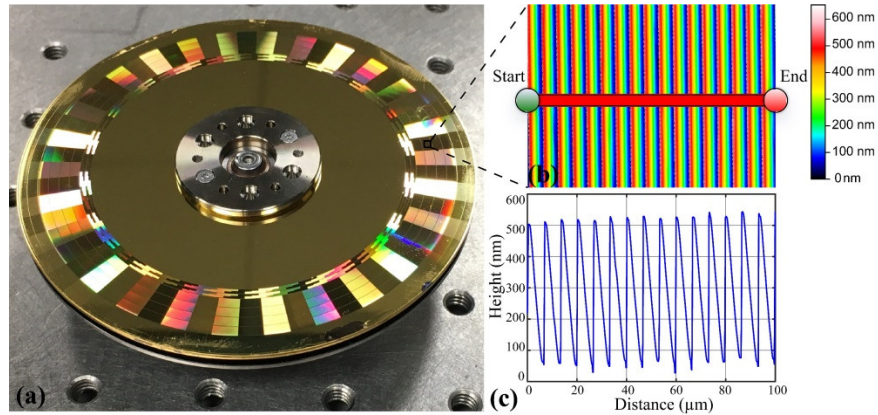


Figure 7. Fabricated element pinwheel with conformal gratings. (a) Photograph of the pinwheel; (b) Top view of the grating pattern in the area marked in (a); (c) Line profile of the grating along the red bar in (b).

The pinwheel was characterized by using a 3D optical profilometer to measure the surface profiles and roughness of the conformal grating. As shown in Fig. 7(b), the top view of the grating pattern which corresponds to the square area in Fig. 7(a), and the line profile along the red bar is drawn in Fig. 7(c). As we can see, the grating is relatively uniform and smooth. The average of grating period is about 6.63 μm, which is very close to the desired value. The grating also shows flyback regions, which may be caused by the limited spatial resolution of the laser, and will primarily impact the diffraction efficiency of the pinwheel from the near-zero center wavelength loss of high quality ruled gratings.

To measure the diffraction efficiency of the pinwheel, a laser at 1310 nm is used as the light source, and a photodiode power sensor is put in front of the pinwheel to detect the optical power of the diffracted beam. We measured the diffraction efficiency of all 56 grating sectors by spinning up the pinwheel and detecting the output beam in four directions (up, right, down, left), respectively. The measured diffraction efficiency of one track under horizontal and vertical polarizations are shown in Fig. 8. The maximum is about 85%, and the minimum is about 70%. The curves reflect some fluctuations of diffraction efficiency, which is due to variations in the laser written surface profile as well as aliasing with respect to the pixel grid. And the efficiency loss is mainly suffered from the flyback effect as we showed in Fig. 7. Comparing Fig. 8(a) and (b), there is a small change in the diffraction efficiency, i.e., the diffraction efficiencies of up and down directions are lower in P polarization but higher in S polarization, and similar change appears in right and left directions. Because these changes are small, we find the pinwheel scanner to be largely polarization insensitive, at least for the fabricated scan angles.

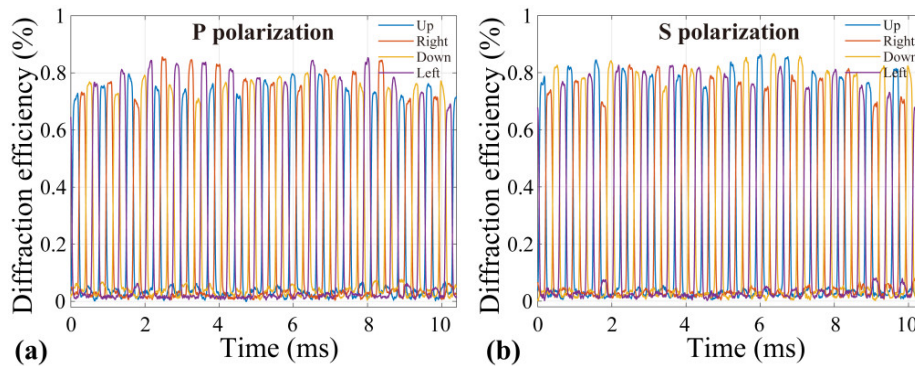


Figure 8. Diffraction efficiency of 56 grating sectors under (a) P polarization and (b) S polarization.

Figure 9 shows the quasi-static beam steering of the pinwheel rotating at 7200 rpm, as well as the beam switching speed under different incident beam sizes. The input Gaussian beam is truncated by an iris diaphragm to obtain several beam diameters: 1.4mm, 1.2mm, 1.0mm, and 0.8mm. The intensities are normalized, and the switching time is determined by the time difference between  $t_1$  and  $t_2$ , where  $t_1$  is the time when one beam falls to 90% intensity, and  $t_2$  is the time when the next beam rises to 90% intensity. The switching speeds are labeled in the corresponding positions of each figures, which show a very fast switching speed of the pinwheel. The switching is faster as the beam size decreases. The average switching time at 1 mm beam diameter is about 31  $\mu$ s, close to the theoretical value of 33  $\mu$ s. The difference is from the beam width accuracy and imperfect control on the spinning speed of the motor. There are apparent beam vibrations in the dwelling state, which is related to the uniformity of the grating and the mechanical stability of the rotating disk. All of these factors can be refined with modest effort.

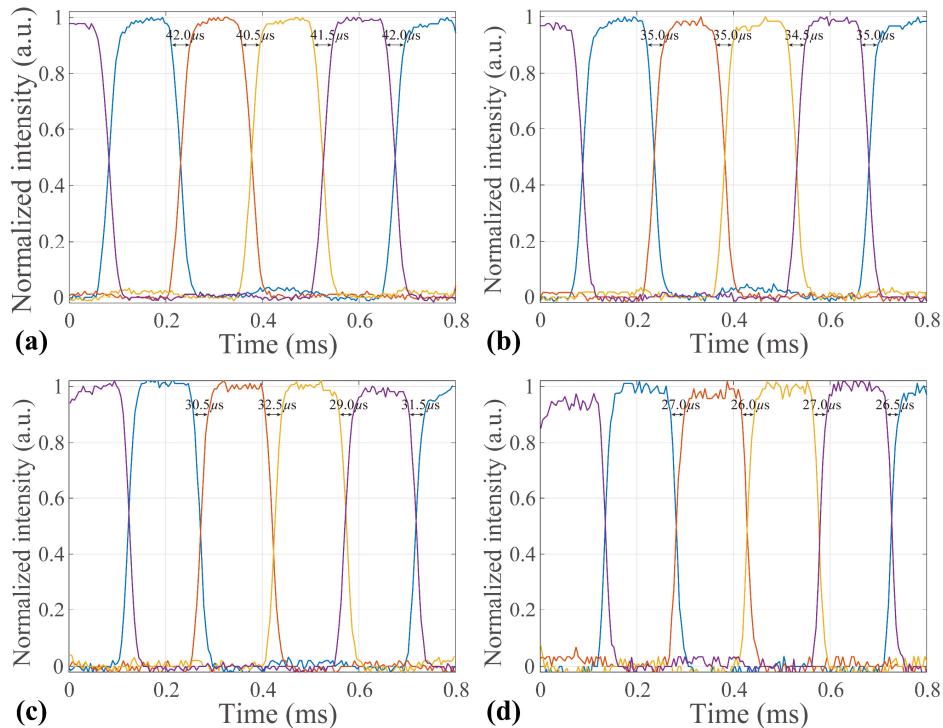


Figure 9. Beam switching time for different incident beam diameters. (a) 1.4mm; (b) 1.2mm; (c) 1.0mm; (d) 0.8mm.

## 5. CONCLUSIONS

We have proposed a novel ‘pinwheel’ scanner to realize fast quasi-static beam steering by using regional conformal mapping of blazed diffraction gratings on a rotating disk, where the beam pointing is stable as the disk rotates within each facet. The theoretical method of conformal mapping is rigorously deduced and carefully implemented in Matlab and Zemax software tools. We fabricated and characterized a pinwheel scanner with 56 conformally-mapped surface relief grating sectors written by optical lithography on a 95 mm diameter disk. This element, rotating at 7200 rpm, provides microsecond transitions and 75% optical efficiency in free-space beam steering.

## ACKNOWLEDGMENTS

L. Wu is grateful to the China Scholarship Council for supporting his study at the University of California, San Diego through the Joint Training PhD Program and Visiting Scholar Program. This work is supported by the Department of Energy through grant ARPA-E DE-AR000084.

## REFERENCES

- [1] Kessel, P. F. V., Hornbeck, L. J., Meier, R. E. and Douglass, M. R., "A MEMS-based projection display," *Proceedings of the IEEE* **86**(8), 1687–1704 (1998).
- [2] Henderson, C. J., Leyva, D. G. and Wilkinson, T. D., "Free space adaptive optical interconnect at 1.25 Gb/s, with beam steering using a ferroelectric liquid-crystal SLM," *Journal of Lightwave Technology* **24**(5), 1989–1997 (2006).
- [3] Schwarz, B., "LIDAR: Mapping the world in 3D," *Nature Photonics* **4**, 429–430 (2010).
- [4] Xu, J., Cua, M., Zhou, E. H., Horie, Y., Faraon, A. and Yang, C., "Wide-angular-range and high-resolution beam steering by a metasurface-coupled phased array," *Opt. Lett.*, OL **43**(21), 5255–5258 (2018).
- [5] McManamon, P. F. and Ataei, A., "Progress and opportunities in optical beam steering," *Quantum Sensing and Nano Electronics and Photonics XVI* **10926**, 1092610, International Society for Optics and Photonics (2019).
- [6] Wang, Y., Zhou, G., Zhang, X., Kwon, K., Blanche, P.-A., Triesault, N., Yu, K. and Wu, M. C., "2D broadband beamsteering with large-scale MEMS optical phased array," *Optica*, OPTICA **6**(5), 557–562 (2019).
- [7] He, Z., Gou, F., Chen, R., Yin, K., Zhan, T. and Wu, S.-T., "Liquid Crystal Beam Steering Devices: Principles, Recent Advances, and Future Developments," *Crystals* **9**(6), 292 (2019).
- [8] Heck, M. J. R., "Highly integrated optical phased arrays: photonic integrated circuits for optical beam shaping and beam steering," *Nanophotonics* **6**(1), 93–107 (2017).
- [9] Gu-Stoppel, S., Lisek, T., Fichtner, S., Funck, N., Eisermann, C., Lofink, F., Wagner, B. and Müller-Groeling, A., "A highly linear piezoelectric quasi-static MEMS mirror with mechanical tilt angles of larger than 10°," *MOEMS and Miniaturized Systems XVIII* **10931**, 1093102, International Society for Optics and Photonics (2019).
- [10] Janschek, K., Sandner, T., Schroedter, R. and Roth, M., "Adaptive Prefilter Design for Control of Quasistatic Microscanners," *IFAC Proceedings Volumes* **46**(5), 197–206 (2013).
- [11] Mellette, W. M. and Ford, J. E., "Scaling Limits of MEMS Beam-Steering Switches for Data Center Networks," *Journal of Lightwave Technology* **33**(15), 3308–3318 (2015).
- [12] Yan, J., Li, Y. and Wu, S.-T., "High-efficiency and fast-response tunable phase grating using a blue phase liquid crystal," *Opt. Lett.*, OL **36**(8), 1404–1406 (2011).
- [13] Lin, Y.-H., Mahajan, M., Taber, D., Wen, B. and Winker, B., "Compact 4 cm aperture transmissive liquid crystal optical phased array for free-space optical communications," *Free-Space Laser Communications V* **5892**, 58920C, International Society for Optics and Photonics (2005).
- [14] Wyant, J. C., "Rotating Diffraction Grating Laser Beam Scanner," *Appl. Opt.*, AO **14**(5), 1057–1058 (1975).
- [15] Jia, J., Chen, J., Yao, J. and Chu, D., "A scalable diffraction-based scanning 3D colour video display as demonstrated by using tiled gratings and a vertical diffuser," *Scientific Reports* **7**, 44656 (2017).
- [16] Marshall, G. F. and Stutz, G. E., [Handbook of Optical and Laser Scanning], CRC Press (2018).
- [17] Nehari, Z., [Conformal Mapping], Courier Corporation (2012).
- [18] Alvarado, C. and Amore, P., "Spectroscopy of annular drums and quantum rings: Perturbative and nonperturbative results," *Journal of Mathematical Physics* **52**(6), 063516 (2011).
- [19] "Zemax OpticStudio Knowledgebase - Zemax",  
<<https://customers.zemax.com/os/resources/learn/knowledgebase>> (2019).
- [20] Welford, W. T., [Aberrations of Optical Systems], Routledge (2017).